Nanoscale Visualization of Reversible Redox Pathways in Lithium-Sulfur Battery Using In Situ AFM-SECM

Journal of The Electrochemical Society, 2022 **169** 060501
1945-7111/2022/169(6)/060501/8/$40.00 © 2022 The Electrochemical Society ("ECS"). Published on behalf of ECS by IOP Publishing Limited

Nanoscale Visualization of Reversible Redox Pathways in Lithium-Sulfur Battery Using In Situ AFM-SECM

Naresh Kumar Thangavel, Kiran Mahankali, and Leela Mohana Reddy Arava[z]

Department of Mechanical Engineering, Wayne State University, Detroit, Michigan 48202, United States of America

Deducing the electrochemical activity of intermediates and providing materials solution to alter their reaction pathways holds the key for developing advanced energy storage systems such as lithium-sulfur (Li-S) batteries. Herein, we provide mechanistic perspectives of the substrate guided reaction pathways of intermediate polysulfides and their correlation to the redox activity of discharge end products using In Situ atomic force microscopy-based scanning electrochemical microscopy (AFM-SECM) coupled Raman spectroscopy at nanoscale spatiotemporal resolution. In Situ SECM intermediate detection along with Raman analysis at the electrode/electrolyte interface reveals that the precipitation of Li_2S can occur via an electrochemically active lithium disulfide (Li_2S_2) intermediate step. With a detailed spectro-electrochemical and morphological mapping, we decipher that the substrate-dependent Li_2S_2 formation adversely affects the Li_2S oxidation in the subsequent cycles, thereby reducing the round-trip efficiency and overall performance of the cell. The present study provides nanoscale-resolved information regarding the polysulfide reaction pathways in Li-S batteries with respect to the electrode structure and its properties.
 [DOI: 10.1149/1945-7111/ac70ff]

Manuscript submitted November 20, 2021; revised manuscript received February 27, 2022. Published June 1, 2022.

Supplementary material for this article is available online

Understanding of fundamental operating principles across various length scales, *atomistic, single-particle, and mesoscale* has fueled remarkable innovations in lithium-ion battery technologies, driving applications as diverse as electric vehicles, portable electronics, and power grid storage.[1,2] Among many emerging Li-ion based energy storage systems, lithium-sulfur (Li-S) is the most sought-after technology due to its high energy density and low cost.[3,4] However, its performance is guided by highly complex and non-equilibrium conversion reactions of several sulfur intermediates, known as lithium polysulfides (LiPS), along with solid-liquid-solid phase transformations at the cathode surface. Such Li-S batteries often face formidable challenges like rapid capacity fade, sluggish reaction kinetics, short cycle life, and poor coulombic efficiency.[5–8] Despite some success in mitigating these issues by employing a variety of cathode surface modifications,[9–17] the fundamental understanding of LiPS reaction pathways (Some crucial reactions are elucidated in the following Eqs. 1–8) towards discharge end-products (Li_2S_2/Li_2S)[18,19] and their relation to the cathode surface are still not well established.

$$S_8 + 2Li^+ + 2e^- \rightarrow Li_2S_8 \quad [1]$$

$$Li_2S_8 + 2Li^+ + 2e^- \rightarrow Li_2S_6 + Li_2S_2 \quad [2]$$

$$Li_2S_8 + 2Li^+ + 2e^- \rightarrow Li_2S_4 \quad [3]$$

$$Li_2S_6 \rightarrow LiS_3^{*-} \quad [4]$$

$$LiS_3^{*-} + Li^+ + e^- \rightarrow Li_2S_3 \quad [5]$$

$$Li_2S_3 + Li_2S_4 \rightarrow Li_2S_6 + Li_2S \quad [6]$$

$$Li_2S_4 + 2Li^+ + 2e^- \rightarrow Li_2S_2 \quad [7]$$

$$Li_2S_4 + 2Li^+ + 4e^- \rightarrow Li_2S \quad [8]$$

It is commonly believed that the morphology and physicochemical characteristics of the discharge products (Li_2S/Li_2S_2) can be closely correlated to the deteriorating performance issues like internal resistance buildup and capacity fade in Li-S cell.[20–22] Though several spectroscopic techniques have pointed out the critical role of solvents on different LiPS formation and their effect on endproducts,[18,23–29] the studies have presented contrary and speculative results in the case of the existence of lithium disulfide (Li_2S_2). The existence of intermediate Li_2S_2 slows down the deposition kinetics of Li_2S, during the discharge process;[30,31] it should be noted that three-quarters of the cell capacity originates during the Li_2S deposition.[28,29,32–34] However, the role of the Li_2S_2 species in the interfacial process of such high capacity Li_2S precipitation reaction is still highly uncertain, and its contribution to the overall charge/discharge process remains unclear. Such an impasse is due to the practical difficulty in isolating Li_2S_2 intermediates to detect and characterize them experimentally. The complexity further increases, as Li_2S_2 inherently undergoes spontaneous reaction to form Li_2S, according to the thermodynamic principles and Li-S phase diagram,[35,36] making it virtually impossible to detect by any of the contemporary In Situ techniques.

Recently, by employing atomic force microscopy-based scanning electrochemical microscopy (AFM-SECM) technique, we have demonstrated heterogeneity in the oxidation of the discharge end products (Li_2S/Li_2S_2) of Li-S battery through simultaneous mapping of their electrochemical activity and topography at nanoscale spatial resolution.[37] However, a comprehensive understanding of the factors leading to the precipitation of certain species causing such heterogeneous electrochemical activity is critical to elucidate the Li-S redox process fully. Herein, given that the SECM tool has previously been employed to detect unstable intermediates generated from electrochemical reactions at the nanogap between tip and substrate,[38–41] we attempted to detect and deduce the electrochemical activity of Li_2S_2 with this powerful tool during the Li-S discharge process. Further, the fundamental reason behind the formation of Li_2S_2 species and their influence on the subsequent redox process was evidenced by In Situ Raman spectroscopy. Finally, the electrochemical and morphological aspects associated with Li_2S_2 species were investigated by AFM-SECM mapping. In this work, we establish a surface–activity relationship of cathodes in controlling the LiPS redox pathways and charge/discharge end product deposition. With this knowledge, we also provide a materials-based solution that could guide the efficient LiPS redox reaction pathways to enhance the reversibility of Li-S cells.

Experimental

Materials.—Lithium foil (Li, 99.9%, Alfa Aesar), Lithium sulfide (Li_2S, 99.98%, Sigma), Sulfur (99.998%, Sigma), Tetraethylene

[z]E-mail: leela.arava@wayne.edu

glycol dimethyl ether (TEGDME, 99%, Sigma), Lithium bis(trifluoromethanesulfonyl)imide (LiTFSI, 99.95%, Sigma), Lithium nitrate ($LiNO_3$, 99.99%, Sigma), Bis(cyclopentadienyl)cobalt (Cobaltocene, Alfa Aesar), Chloroplatinic acid hydrate (H_2PtCl_6. xH_2O, 99.9%, Sigma), Sodium sulfate (Na_2SO_4, >99%, Sigma), Nickel (II) sulfate hexahydrate ($NiSO_4$. $6H_2O$), >98%, Sigma) were used without any further purification. Glassy carbon (5 mm × 4 mm, Ted Pella) was polished with alumina paste and was washed thoroughly with DI water before each experiment.

Lithium polysulfides (catholyte) preparation.—Stock solutions (0.2 M) of Li_2S_8, Li_2S_6, and Li_2S_4 were prepared by mixing stoichiometric amounts of Li_2S and sulfur in TEDGME solvent with active stirring at 90 °C overnight. A blank solution containing 0.1 M-LiTFSI and 0.1M- $LiNO_3$ in the TEGDME solvent was also prepared similarly without heating. Stock solutions were diluted in blank electrolyte appropriately for each experiment.

Electrolyte for approach curve studies.—For SECM approach curve studies, 2 mM Cobaltocene in 0.1 M-LiTFSI and 0.1M-$LiNO_3$ in the TEGDME solvent was used.

AFM-SECM experimental set up & cell assembly.—The entire setup was placed on an i4 series active vibration isolation table (Accurion Ltd), to suppress any external vibrations and disturbances. The AFM-SECM tip functioning was monitored by NSW software, supplied by Nanonics Ltd, while electrochemical measurements were monitored by both NSW and CHI software. The AFM-SECM platinum (Pt) nanoprobes used in this study were procured from the Nanonics company and had a radius of 50 nm with an Rg factor of 3 and Q-factor of 1405. A frequency of 32.55 kHz was used for tuning the AFM probe to obtain an approach. A specially designed four-electrode electrochemical cell was used for the AFM-SECM cell setup. Herein, the AFM-SECM platinum (Pt) tip was used as working electrode-1 (WE 1) while a modified glassy carbon circular disk, served as working electrode-2 (WE 2). A lithium strip acted as a reference cum counter electrode. For the electrolyte, the concentration of Li salt was pinned as 0.1 M LiTFSI with 0.1 M $LiNO_3$ as an additive and TEGDME as the solvent for all the studies.[22,37,42] The cell was assembled inside an Argon filled glove box (with oxygen and moisture levels below 0.1 ppm) in a specially designed transfer chamber equipped with provisions to circulate Argon gas. After the cell assembly, the chamber was sealed thoroughly inside the glovebox and was transferred to the AFM-SECM work-station. A constant Argon gas flow was maintained in the environmental chamber, during all the studies, to maintain a highly controlled atmosphere required for the Li-ion battery experiments.

Insitu raman measurement.—The In-situ Raman measurements were carried out in an ANDOR Shamrock 500i model system using a 532 nm green laser (Nd:YAG source). Further, a specially designed liquid immersion 40 ×/0.80 w objective lens was used for Raman studies to reduce the refractive index mismatch in the optical path caused by the air/electrolyte interface. This lens provides better sensitivity and a high spatial resolution, which assists in an accurate measurement. The laser power utilized for all the measurements is 50 mW from which only 10% was utilized for recording the spectrum; a grating number of 600 (600 grooves/mm) with an accumulation time of 30 s was used. Raman studies were governed by Solis software provided by ANDOR.

Results & Discussion

In situ SECM SG-TC mode detection of Li_2S_2 intermediate.—Herein, AFM feedback-controlled SECM tip approach and functioning enables a reliable tip-to-substrate distance control and provides a nanoscale spatial resolution. Figures 1a, 1b shows the scanning electron microscopy (SEM) and electron backscatter diffraction (EBSD) images of the AFM-SECM Platinum (Pt) tip used in this study. The Pt tip has a conical shape with a diameter of 100 nm and an R_g factor (ratio of glass sheath to tip) of 3. To evaluate the electrochemical performance of the tip, we performed cyclic voltammetry (as shown in Fig. 1c and Supporting Fig. S1b (available online at stacks.iop.org/JES/169/060501/mmedia)) with cobaltocene redox mediator dissolved in non-aqueous solvents. The tip voltammogram showed a well-defined sigmoidal shape with a negligible capacitive current indicating the suitability of the Pt tip for SECM studies. The steady-state current of the AFM-SECM Pt tip recorded far away from the substrate ($i_{T,\infty}$) was found to be 11 pA; and the diffusion coefficient for cobaltocene redox mediator was determined to be 5.7×10^{-7} cm^2 s^{-1} (detailed calculation is provided in SI). Then the current vs distance curve was recorded (Fig. 1d), and the tip current was found to increase gradually from $i_{T,\infty}$ to i_T at the AFM-SECM tip. The experimental curve fits the positive feedback theoretical curve until L = 3.65 (L = *d/a*, where *d* is the distance from the substrate and *a* is the radius of the tip) and the tip-to-substrate distance was found to be 183 nm (approach curve measurement and curve-fitting details are given in SI). The L value obtained here is appropriate to maintain d/a $\gg$ 1 to avoid problems due to interference by the diffusion layers between the substrate and the tip and is suitable for various SECM operating modes like generation-collection and competition.[43]

It has been reported that detection of Li_2S_2 using traditional characterization techniques is highly challenging.[44,45] Based on the fact that Li_2S_2 is electrochemically active compared to Li_2S,[46] here, we have attempted for the electrochemical detection of Li_2S_2 with the help of substrate generation-tip collection (SG-TC) SECM mode as shown in schematic Fig. 2a. Due to the complexity of Li-S reactions, we have chosen Li_2S_4 as the starting material for this study, as it is the only intermediate liquid species present before the formation of Li_2S_2/Li_2S solid species. In SG-TC experiment, the tip potential (E_{tip}) was held constant at 2.1 V vs Li/Li^+ to detect any traces of Li_2S_2, while the substrate potential (E_{sub}) was slowly swept from 2.1 to 2.0 V, at a scan rate of 0.05 mV s^{-1}, the region where Li_2S_4 undergoes reduction. The substrate potential range was determined for detection based on the overpotential measurement (theoretical potential ~ 2.11 V vs Li/Li^+ for Li_2S_2/Li_2S[46]) by galvanostatic intermittent titration technique (GITT, Supporting Figs. S2–S3) and potentiostatic intermittent titration technique (PITT, Supporting Figs. S4–S5) on both carbon and Ni surfaces in LiPS solutions.

Before the Li_2S_2 detection, the voltammetric response of Li_2S_4 on the SECM Pt tip was recorded (Fig. 2b and Supporting Fig. S6) to ascertain the electrode performance and fouling effect on Pt nanoelectrode in the LiPS solution. As shown in cyclic voltammetry (CV), at 1.8 V cut-off, the Pt tip displayed the typical sigmoidal waves at appropriate potentials of Li_2S_4 reduction and oxidation reactions, with a negligible capacitive current. The obtained CV results indicate a reversible Li_2S_4 redox reaction without any solid end product deposition on the tip, in the chosen potential region. This can be attributed to the electrocatalytic effect of Pt on LiPS redox reaction and is in good agreement with the results of previous reports.[16,47] Whereas, at potentials below 1.8 V, huge reduction and corresponding oxidation currents were observed in the tip voltammogram (Supporting Fig. S6a). Such a voltammogram feature is certainly attributed to the Li_2S solid particle deposition and oxidation on the SECM tip. In light of these results, the fouling of Pt nanoelectrode surface due to the sulfur reactions is not expected in this study, as the potential range probed is >1.8 V.

Figures 2c, 2d illustrate the results of SG-TC detection experiments using an AFM-SECM Pt tip close to carbon and nickel (Ni) surface in the event of reduction of Li_2S_4 to Li_2S_2/Li_2S (Figs. S7a and S7b depicts the tip currents recorded on carbon and Ni surfaces with error bars, respectively). Here, it is noteworthy that, several metals were previously proven to be catalytically active towards polysulfide redox, including Pt, Ni etc.[16,48] In the current work Ni has been chosen as a model compound and has been employed as a catalytic surface. As both carbon and Ni surfaces begin to reduce the

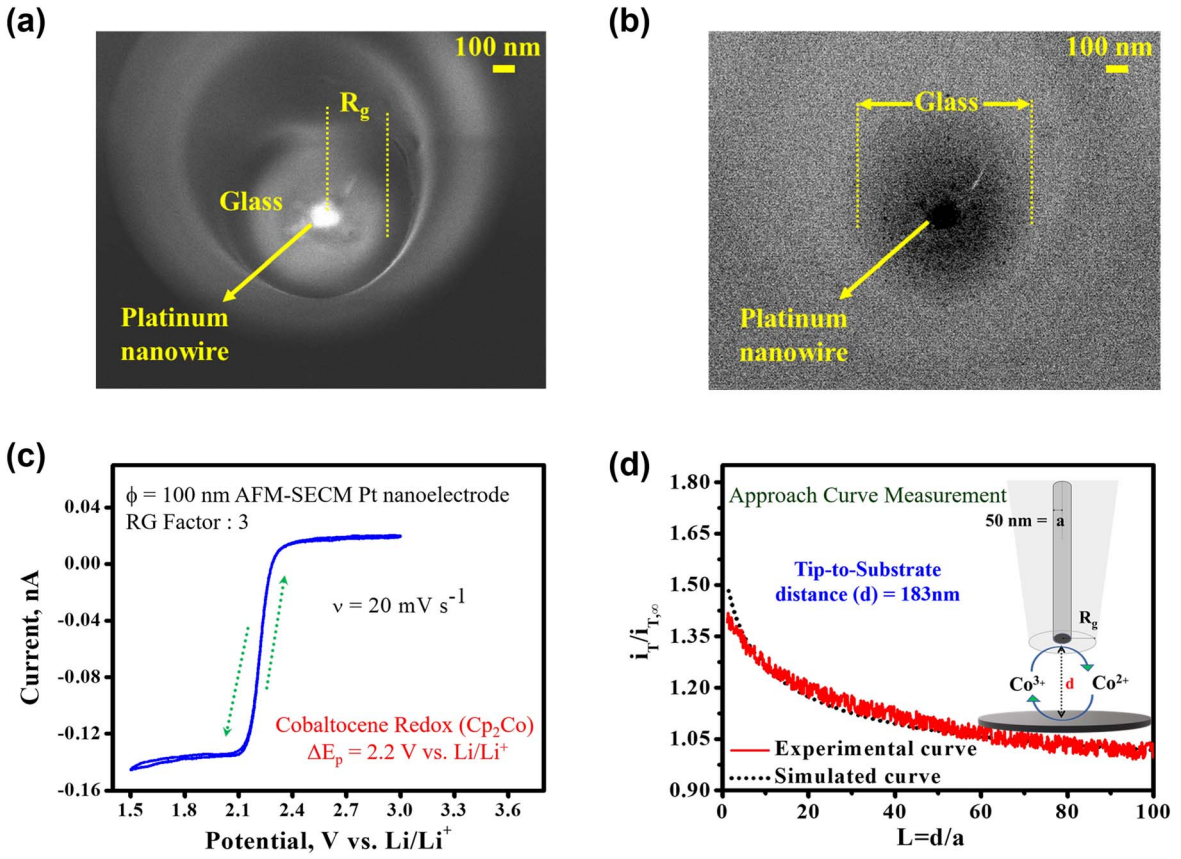

Figure 1. (a) and (b) SEM and EBSD image of AFM-SECM Platinum tip [diameter 100nm and RG factor 3] used in this study. (c) AFM-SECM Pt tip steady state current far away from the substrate recorded in cobaltocene redox mediator (d) i_T – d steady state approach curve [Inset schematic representation of approach curve measurements] Tip biased at reduction potential of 2.1 V and substrate biased at oxidation potential (2.4 V) conditions. Approach performed using a stepper motor at a speed of 0.0003 μm ms^{-1}.

Li_2S_4, the substrate current started to increase (black line). On the other hand, a rise in faradaic tip current was observed on the carbon surface, when potential reaches ~2.05 V, which then decreases when the substrate potential becomes sufficiently high for Li_2S nucleation. The increases in tip current can be correlated to the oxidation of detected electrochemically active Li_2S_2 in the diffusion layer during Li_2S_4 to Li_2S transition. Further, an initial increase followed by a decrease in the tip current on the carbon surface can be attributed to the continuous formation of Li_2S_2 and immediate further reduction into Li_2S. Though such trends were occasionally observed in non-battery systems such as detection of peroxide and borohydride intermediate,[40,41] they were never reported in the Li-S system. Remarkably, on the Ni surface, a stable tip current was observed without any signs of faradic current, which demonstrates that there is no formation of electrochemically active (Li_2S_2) intermediate product. Based on these observations, we deduce that Li_2S_4 is directly converted into Li_2S on a catalytically active Ni surface without the formation of the Li_2S_2 intermediate. These results demonstrate that Li_2S_2 formation depends upon the nature of the cathode surface and indicates that the LiPS redox pathways follow different routes during the discharge process.

Cathode surface dependent evolution of intermediate polysulfides by in situ Raman analysis.—To corroborate the existence of Li_2S_2 and to understand the role of cathode surface on the evolution of intermediate LiPS species during the discharge process, we have performed In Situ Raman spectroscopic studies. Herein, to precisely track the short-lived intermediates at the cathode/electrolyte interface, we have employed a specially designed liquid immersion objective lens which provides sub-micrometer spatial (0.8 μm) resolution.[37,49,50] Figures 3a, 3b shows Raman spectra obtained on carbon and Ni cathode surfaces during discharge from 2.4 to 1.5 V vs Li/Li$^+$. Herein, the Raman peak assignments for the LiPS species detected during the In Situ experiments, including Li_2S_2 and Li_2S (Table SI), were made based on the reference sample spectrum (Supporting Figs. S8–S10, Table SII) and validated with the previous reports.[21,28,29,33] As the discharge process proceeded, three new peaks at 256, 534, and 234 cm^{-1} start appearing on both surfaces, which correspond to the S_6^{2-}, S_3^{*}, and S_4^{2-} species, respectively. The intensity of the peak corresponding to S_4^{2-} species was comparable on both surfaces and was detected even at a low discharge potential region (1.9 V).[33] However, S_3^{*-} peak intensities increased with increasing depth of discharge and appeared as a strong Raman signal on the Ni surface, whereas only a weak signal was observed on carbon. Further, at a discharge potential of 1.9 V, Raman peaks corresponding to the short-chain LiPS of S_2^{2-} and S_2^{-} can be expected at 514 and 375 cm^{-1}, respectively. Surprisingly, a strong band of S_2^{2-} appeared in the carbon spectrum, suggesting the existence of Li_2S_2 at the midway of discharge. More importantly, the 514 cm^{-1} band continued to appear even at further discharge potentials and persisted even after the final product (Li_2S) formation at 1.7 V on the carbon surface. Whereas, on Ni surface, insignificant Raman features at 514 cm^{-1} indicate the absence of S_2^{2-} and show only Li_2S peak at its corresponding region. The difference in the formation of discharge products and earlier formation of Li_2S from preceding LiPS on Ni (1.9 V) proves the surface effect on intermediate LiPS evolution during Li-S discharge.

Overall, the difference in the evolution of LiPS redox species and their reaction pathways concerning the cathode surface can be explained as follows (Table SIII): On the Ni surface, Li_2S_8 initially undergoes fast disproportionation reaction as confirmed by their corresponding very weak Raman band appearance and produces

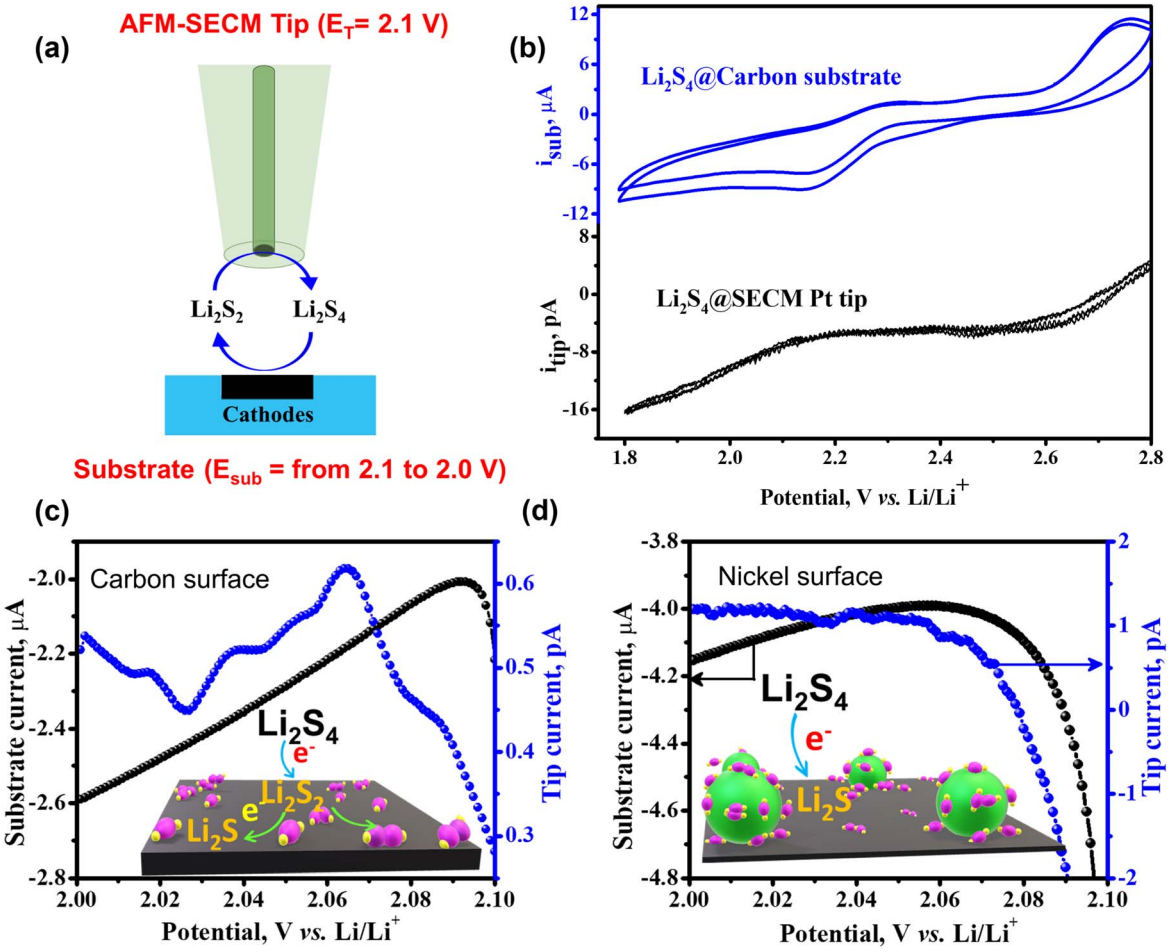

Figure 2. In situ Substrate generation-Tip collection SECM Mode for Li_2S_2: (a) Schematic representation of SG-TC mode of SECM used for intermediates detection during Li-S reduction (b) Cyclic voltammetry on Pt tip and carbon substrate in polysulfide solution in the potential region between 3.0 V to 1.8 V vs Li/Li $^+$ at a scan rate of 0.5 mV; Tip and substrate currents recorded in SG-TC mode by biasing tip at 2.1 V while scanning the substrate from 2.1 V to 2.0 V at a scan rate of 0.5 mV s^{-1} on (c) carbon and (d) nickel surfaces. [Electrolyte: 1 mM Li_2S_4 + 0.1 M LiTFSI + 0.1 M $LiNO_3$ in TEGDME].

Li_2S_6. Then, as formed S_6^{2-} dissociates into tri sulfur radicals, S_3^{*-} which equilibrates with each other until the complete consumption of S_6^{2-}, hence, the existence of strong radical peak suggests that high concentration of S_6^{2-} is present on the Ni surface. The observed results are contrary to previous reports, which stated that the S_6^{2-} the peak was difficult to observe due to their faster conversion reaction kinetics.[18,34] Yet, our results illustrate that the evolution of such intermediate LiPS species and their reactivity during sulfur reduction is dependent on the type of cathode surface employed. The presence of a high concentration of Li_2S_6 on the Ni surface indicates the stabilization of such species, which can be attributed to the polar-polar interactions between them and the Ni surface. Such stabilization of intermediate LiPS, which are known to be predominant species in shuttling phenomena,[16,51] is crucial to mitigate their dissolution and to direct further conversion reactions. At low voltage plateau, as formed S_3^{*-}/S_6^{2-} undergoes electroreduction to generate S_4^{2-} which again equilibrates with S_3^{*-}. Further, with decreasing potential, the presence of S_3^{*-} directs the S_4^{2-} reduction towards disproportionation rather than the electrochemical route, which yields a mixture of S^{2-} and S_6^{2-}. Whereas, on the carbon surface at discharge voltages below 2.3 V, Li_2S_8 undergoes a swift disproportionation reaction to produce S_4^{2-} instead of S_6^{2-} indicating that S_4^{2-} is the most predominant species. This is further corroborated by observing a negligible concentration of free radical and hence a low concentration of S_6^{2-} is expected, which can alter the course of the further reduction process. Subsequently, as formed, S_4^{2-} preferentially undergoes a step-by-step electrochemical reduction to form Li_2S_2 and then to Li_2S at <1.8 V.[19] From the LiPS redox investigated by SG-TC SECM mode assisted by In Situ Raman spectroscopy, we conclude that the reduction product on the conventional carbon electrode consists of both Li_2S_2 and Li_2S, whereas only Li_2S forms on Ni substrate. More importantly, it is observed that the presence of S_3^{*-} radical controls the end product deposition route, and such radical assists in the direct conversion of S_4^{2-} to Li_2S on the Ni surface.

According to the above illustrated reaction pathways of LiPS, the resulting intermediate Li_2S_2 step could alter the deposition kinetics of Li_2S on carbon. To account for this, we carried out In Situ AFM studies on the Li_2S growth process on both carbon and Ni surfaces (Supporting Figs. S12–S14). On the carbon surface, with decreasing potential, a continuous evolution of new nuclei along with the growth of existing ones into small particles at a slow rate was observed, which was previously defined as progressive growth process.[52,53] Whereas on Ni surface, the formation of dense solid particles with larger size was observed, and particles showed negligible changes in height upon changing the potentials, indicating that the formation of new nuclei and the growth process seized. This is further exemplified from the ex situ SEM images of the electrodes which revealed the formation of smaller reduction products on the carbon surface (Supporting Figs. S15a, S15b), while larger particle deposits were observed on the Ni surface (Supporting Figs. S15c, S15d). To gain further insights, potentiostatic discharge curves collected during the Li_2S growth on both surfaces were analyzed (Supporting Figs. S16 and S17 along with corresponding details). It

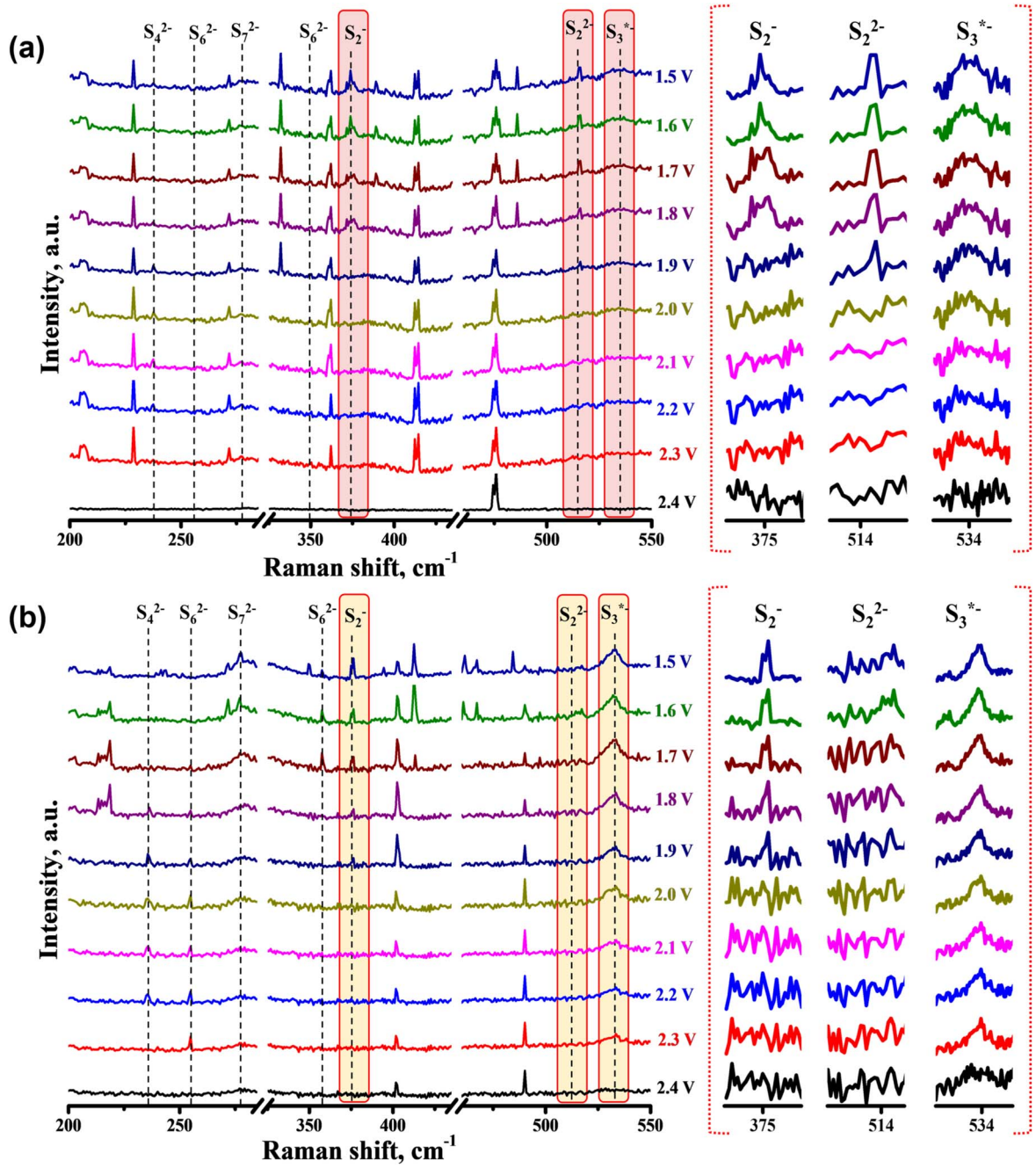

Figure 3. In situ Raman measurements for LiPS redox species evolution on different cathode surface: Laser micro-Raman measurements during Li-S reduction on (a) Carbon (d) Nickel surfaces in the potential ranges of 2.4 V to 1.5 V. [Laser source: 532 nm Nd: YaG green laser].

was found that Li_2S growth proceeds via progressive and instantaneous processes on the carbon and Ni surface respectively. Based on these evidences, we deduce that the formation of intermediate Li_2S_2 renders the growth process of Li_2S continuous and slow, with smaller particle size, on carbon surface. On the other hand, absence of Li_2S_2 encourages instantaneous and limited nuclei formation on the Ni surface which leads to the preferred growth of fewer but larger Li_2S particles and more Li_2S deposited on a given electrode surface area.[52,54]

In Situ AFM-SECM mapping of Li_2S/Li_2S_2 oxidation process.—To understand the oxidation of Li_2S that has formed in the presence of Li_2S_2, we have performed simultaneous topographical and electrochemical mapping by AFM-SECM under oxidative conditions (Fig. 4). Herein, the SECM tip approach to the substrate is governed by the AFM feedback loop rather than electrochemical signal (as in conventional SECM operating mechanism), which enables concurrent measurement of the local electrochemical activity and topographical changes. For electrochemical mapping, we have employed competitive SECM mode to probe the electrochemical activity of Li_2S_2/Li_2S during oxidation. In this mode, both tip and substrate compete for the same electrochemically active intermediate species, as shown in Fig. 4a. During the Li-S charging process, Li_2S oxidation occurs via a two-stage process: (i) conversion of Li_2S to stable and electrochemically active intermediate Li_2S_6; and (ii) further oxidation of Li_2S_6 to S_8^{2-} for subsequent transformation to S_8.[55,56] Since the Li_2S_6 is the only electroactive species present before the formation of the solid end product of charging, we used Li_2S_6 as the redox mediator to establish the competition mode operation of SECM. In this mode, during a typical

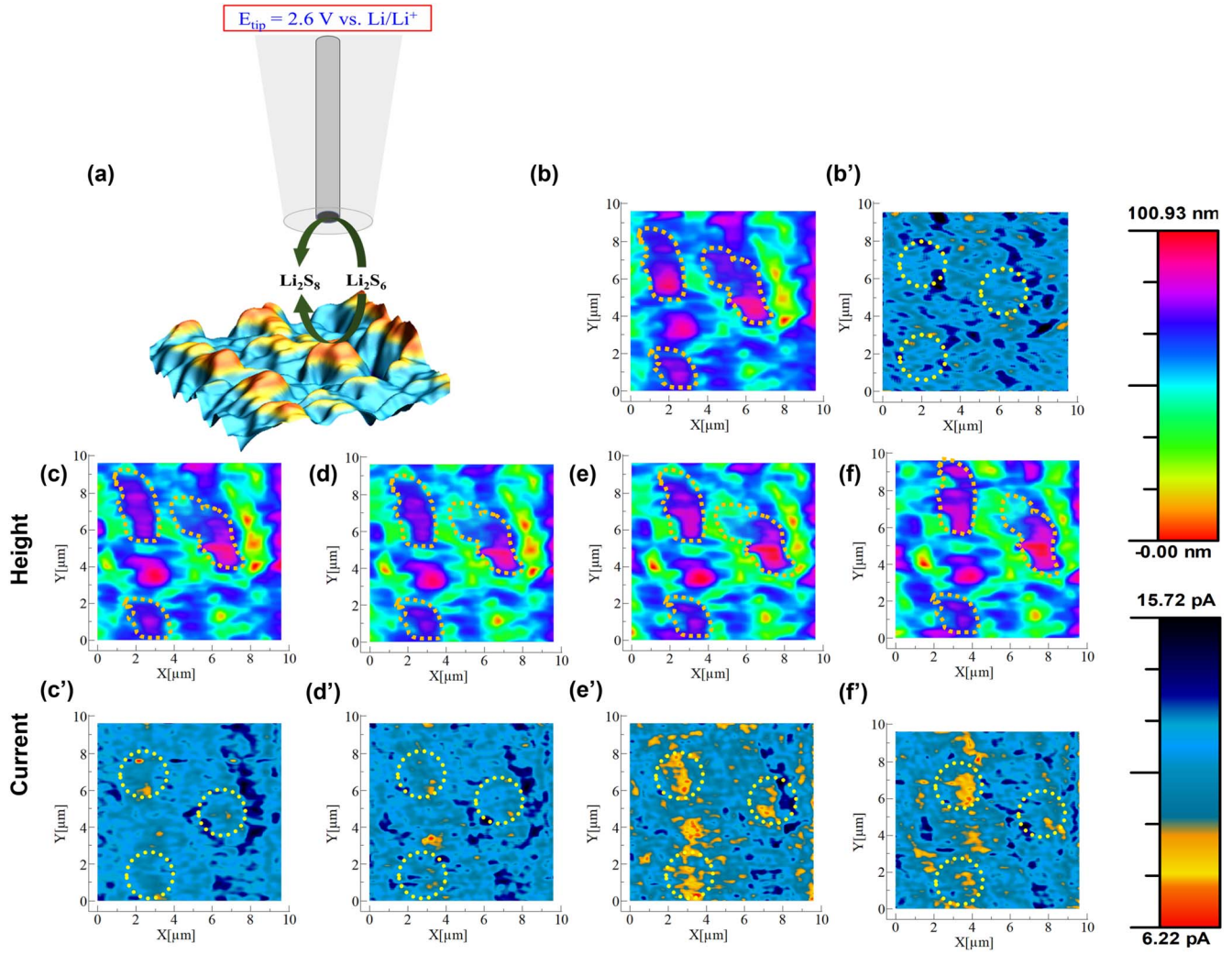

Figure 4. AFM-SECM imaging of Li_2S/Nickel surface during oxidation: (a) Schematic representation of competitive SECM mode of imaging (b), (b′) Height and current mapping of Li_2S [galvanostatically deposited] on glassy carbon before oxidation; Simultaneous height, current mapping of Li_2S surface at substrate potentials of (c), (c′) 2.5 V (d), (d′) 2.6 V (e), (e′) 2.7 V (f), (f′) 2.8 V vs Li/Li$^+$ respectively; E_{tip} = 2.6 V.

scanning, the tip is held at a constant oxidation potential of 2.6 V. In contrast, the substrate potential is tuned between 2.5 and 2.8 V. The potentials for the tip and substrates are chosen based on the CV response recorded on both the tip and the corresponding substrates in LiPS solutions. At substrate potentials, ⩾2.6 V, both the tip and substrate, compete for the conversion of Li_2S_6, resulting in a reduced tip current at locations where the substrate consumes the species. Such a decrease in tip current assists in the identification of highly active regions on the cathode. Before the oxidation studies, we have performed a control experiment for the competition mode to demonstrate its applicability for imaging the Li-S system (details provided in SI, Supporting Fig. S18). The results validate the experimental setup, and the analysis reported herein.

To obtain distinguishable surface features with AFM-SECM mapping, controlled deposition of Li_2S_2/Li_2S was carried out on carbon and Ni surfaces (the corresponding experimental details are provided in SI, and the topographic images are given presented in Supporting Figs. S19–S21). Figure 4 presents the simultaneously recorded height (Figs. 4c–4f) and current images (Figs. 4c′–4f′) of Li_2S oxidation on the Ni surface at different potentials, and the corresponding histograms are presented in Supporting Fig. S22. When a potential of 2.5 V was applied to the substrate, the overall height of all the particles decreased, indicating the initiation of the oxidation process of the as-formed Li_2S (Fig. 4c). The corresponding current image depicts uniform tip current throughout the surface even on the Ni particles (Fig. 4c′), demonstrating that tip functioning is not influenced by the surface as required to operate SECM in competition mode. By raising the substrate potential to 2.6 V, the height of certain particles (as marked by a yellow circle) was found to decrease further; while displaying minimal tip current changes on them (Figs. 4d, 4d′). Interestingly, at substrate potentials greater than 2.7 V, particle re-emergence (Figs. 4e, 4f) and decrease in tip currents (as marked by a yellow circle, Figs. 4e′, 4f′) were observed on the locations where height decrement was previously noted (Figs. 4b, 4c). The decreased tip current on the particles indicates the efficient consumption of as formed LiPS for the re-deposition of solid products, which is reflected by height increment in the topographic images. However, in the case of carbon surface (Supporting Figs. S23, S24), simultaneous shrinkage of some particles (marked by black circles) along with the growth of certain particles at different locations (marked by black circles) was observed at an oxidation potential of 2.6 V. At this potential, decreased tip currents were recorded, on the particles which displayed growth in height along with some random locations on the substrate (Supporting Figs. S23b, b′). At subsequent potentials (⩾ 2.7 V) further increase in the height of the particles (Supporting Fig. S23 c, d) and decreased tip currents (Supporting Figs. S23c′, d′) was observed. Unlike the Ni surface, a decrease in tip current at

2.6 V was seen on arbitrarily growing solid particles with simultaneous dissolution in some locations, which establishes the surface dependent interfacial behavior of LiPS reactions.

The marked difference in topography and tip current behavior on carbon and Ni surfaces can be explained as follows. During the first stage of oxidation on the carbon surface, the electrochemically active Li_2S_2 particle deposits can readily oxidize, compared to inherently insulating Li_2S particles, to produce intermediate liquid Li_2S_6. Owing to the inability of carbon to trap the as-formed Li_2S_6, it tends to diffuse away from its originating location to the neighboring regions or migrate away from the surface. These Li_2S_6 can preferably interact with unoxidized Li_2S due to its strong adsorption energy[57] to undergo chemical/electrochemical reactions at higher oxidation potentials, thus resulting in the particle growth. Due to such interfacial process, while scanning, decrease in tip current along with a simultaneous increase in the particle height was observed as early as 2.6 V. The interaction of intermediate LiPS with Li_2S visualized here validates the previously proposed Li-S charging mechanism using X-ray absorption spectroscopy studies.[56] Whereas on Ni surface, the oxidation of Li_2S particles yields intermediate Li_2S_6, as indicated by a decrement in the height of the particles at 2.5 V. Besides, fading away of the particles until 2.6 V indicates a continuing oxidation process of Li_2S to Li_2S_6 conversion. However, in contrast to the carbon surface, electrocatalytically active Ni surface exhibits a great binding affinity towards the LiPS, which enables their stabilization and further oxidation at the same location. This was corroborated by the increase in the height of the particles with a decrease in the corresponding tip current from 2.7 V. With the information revealed by AFM topography and SECM current images presented in this study, we infer that the presence of Li_2S_2 has the following effects: (i) it plays a predominant role in the deposition of charge/discharge end products at different locations; (ii) it leads to non-uniform deposition of charging end products on unoxidized Li_2S, which favors the growth of insulating parts. Thus, over cycling, this process of formation of alternate layers of Li_2S and charge products finally leads to an increase in the contact resistance between the active material and the substrate owing to the insulating nature of Li_2S (which hinders the charge transfer[58]) thereby leading to capacity fade.

Conclusions

In summary, for the first time, we have successfully detected the Li_2S_2 intermediate species in the Li-S redox system using the substrate generation- tip collection (SG-TC) SECM experiment. The obtained results show that Li_2S_2 species formed on carbon while it is absent on polar host substrates such as nickel. Further, In Situ Raman spectroscopy measurements elucidated the possible root cause for the formation of Li_2S_2 during LiPS redox on both the carbon and Ni surfaces. With a detailed analysis, we conclude that Li_2S_4 electrochemical reduction reactions pave a way to the deposition of Li_2S_2 in addition to Li_2S on carbon. Whereas, Li_2S_4 disproportionation leads to direct Li_2S deposition on the Ni surface. In Situ AFM-SECM topography and electrochemical mapping reveal that the presence of Li_2S_2 on the carbon surface dictates the non-uniform deposition of discharge/charge end products during cycling. Interestingly, on the Ni surface, the oxidation process was found to be confined to the catalytically active Ni surface, thereby resulting in a systematic deposition of charge/discharge end products. Thus, the demonstrated mechanistic understanding of LiPS redox reactions, in Li-S cells, will guide researchers to develop more suitable cathode materials that can deal with the intricacies due to Li_2S precipitation and its reversibility.

Acknowledgments

This material is based upon work supported in part by the National Science Foundation under grant no. 1751472 and ACS Petroleum Research Fund (ACSPRF: 57647-DNI10). The authors thank the Lumigen Instrument Centre at Wayne State University for the use of JSM-7600 FE-SEM (NSF: MRI 0922912) facility. N.K.T. would like to thank Dr. K.L.N. Phani, CSIR-Emeritus Scientist, IICT-Hyderabad, India, who provided constant motivation and helpful discussions during these studies.

ORCID

Naresh Kumar Thangavel https://orcid.org/0000-0002-6604-0211
Kiran Mahankali https://orcid.org/0000-0003-3540-5350
Leela Mohana Reddy Arava https://orcid.org/0000-0001-6685-6061

References

1. C. P. Grey and J. M. Tarascon, *Nat. Mater.*, **16**, 45 (2016).
2. J. Lu, T. Wu, and K. Amine, *Nat. Energy*, **2**, 17011 (2017).
3. A. Manthiram, Y. Fu, S. H. Chung, C. Zu, and Y. S. Su, *Chem. Rev.*, **114**, 11751 (2014).
4. P. G. Bruce, S. A. Freunberger, L. J. Hardwick, and J. M. Tarascon, *Nat. Mater.*, **11**, 19 (2012).
5. R. Xu, J. Lu, and K. Amine, *Adv. Energy Mater.*, **5**, 1500408 (2015).
6. A. Manthiram, Y. Fu, and Y. S. Su, *Acc. Chem. Res.*, **46**, 1125 (2013).
7. G. Zhang, Z. W. Zhang, H. J. Peng, J. Q. Huang, and Q. Zhang, *Small Methods*, **1**, 1700134 (2017).
8. M. Wild, L. O'neill, T. Zhang, R. Purkayastha, G. Minton, M. Marinescu, and G. Offer, *Energy. Enviro. Sci.*, **8**, 3477 (2015).
9. D. Liu, C. Zhang, G. Zhou, W. Lv, G. Ling, L. Zhi, and Q. H. Yang, *Adv. Sci.*, **5**, 1700270 (2018).
10. H. J. Peng, G. Zhang, X. Chen, Z. W. Zhang, W. T. Xu, J. Q. Huang, and Q. Zhang, *Angew. Chem. Int. Ed.*, **55**, 12990 (2016).
11. G. Babu, N. Masurkar, H. Al Salem, and L. M. Arava, *J. Am. Chem. Soc.*, **139**, 171 (2017).
12. Y. S. Su, Y. Fu, T. Cochell, and A. Manthiram, *Nat. Commun.*, **4**, 2985 (2013).
13. X. Tao et al., *Nat. Commun.*, **7**, 11203 (2016).
14. Q. Pang, D. Kundu, M. Cuisinier, and L. Nazar, *Nat. Commun.*, **5**, 4759 (2014).
15. Q. Pang, X. Liang, C. Y. Kwok, and L. F. Nazar, *Nat. Energy*, **1**, 16132 (2016).
16. H. Al Salem, G. Babu, C. V. Rao, and L. M. Arava, *J. Am. Chem. Soc.*, **137**, 11542 (2015).
17. K. Mahankali, N. K. Thangavel, D. Gopchenko, and L. M. R. Arava, *ACS Appl. Mater. Interfaces*, **12**, 27112 (2020).
18. C. Barchasz, F. Molton, C. Duboc, J. C. Lepretre, S. Patoux, and F. Alloin, *Anal. Chem.*, **84**, 3973 (2012).
19. Q. Wang, J. Zheng, E. Walter, H. Pan, D. Lv, P. Zuo, H. Chen, Z. D. Deng, B. Y. Liaw, and X. Yu, *J. Electrochem. Soc.*, **162**, A474 (2015).
20. J. Yan, X. Liu, and B. Li, *Adv. Sci.*, **3**, 1600101 (2016).
21. Y. Diao, K. Xie, S. Xiong, and X. Hong, *J. Electrochem. Soc.*, **159**, A1816 (2012).
22. S. Y. Lang, Y. Shi, Y. G. Guo, D. Wang, R. Wen, and L. J. Wan, *Angew. Chem. Int. Ed.*, **55**, 15835 (2016).
23. D. Zheng, X. R. Zhang, C. Li, M. E. McKinnon, R. G. Sadok, D. Y. Qu, X. Q. Yu, H. S. Lee, X. Q. Yang, and D. Y. Qu, *J. Electrochem. Soc.*, **162**, A203 (2015).
24. J. T. Yeon, J. Y. Jang, J. G. Han, J. Cho, K. T. Lee, and N. S. Choi, *J. Electrochem. Soc.*, **159**, A1308 (2012).
25. J. Hannauer, J. Scheers, J. Fullenwarth, B. Fraisse, L. Stievano, and P. Johansson, *Chem. Phys. Chem.*, **16**, 2755 (2015).
26. A. Kawase, S. Shirai, Y. Yamoto, R. Arakawa, and T. Takata, *Phys. Chem. Chem. Phys.*, **16**, 9344 (2014).
27. Y. Diao, K. Xie, S. Z. Xiong, and X. B. Hong, *J. Electrochem. Soc.*, **159**, A421 (2012).
28. H. L. Wu, L. A. Huff, and A. A. Gewirth, *ACS Appl. Mater. Interfaces*, **7**, 1709 (2015).
29. M. Hagen, P. Schiffels, M. Hammer, S. Dörfler, J. Tübke, M. J. Hoffmann, H. Althues, and S. Kaskel, *J. Electrochem. Soc.*, **160**, A1205 (2013).
30. P. Partovi-Azar, T. D. Kuehne, and P. Kaghazchi, *Phys. Chem. Chem. Phys.*, **17**, 22009 (2015).
31. X. Yang, X. Gao, Q. Sun, S. P. Jand, Y. Yu, Y. Zhao, X. Li, K. Adair, L. Y. Kuo, and J. Rohrer, *Adv. Mater.*, **31**, 1901220 (2019).
32. M. Helen, M. A. Reddy, T. Diemant, U. Golla-Schindler, R. J. Behm, U. Kaiser, and M. Fichtner, *Sci. Rep.*, **5**, 12146 (2015).
33. W. Zhu, A. Paolella, C. S. Kim, D. Liu, Z. Feng, C. Gagnon, J. Trottier, A. Vijh, A. Guerfi, and A. Mauger, *Sustain. Energy. Fuels*, **1**, 737 (2017).
34. Q. Zou and Y. C. Lu, *J. Phys. Chem. Lett.*, **7**, 1518 (2016).
35. J. W. Dibden, J. W. Smith, N. Zhou, N. Garcia-Araez, and J. Owen, *Chem. Commun.*, **52**, 12885 (2016).
36. H. Park, H. S. Koh, and D. J. Siegel, *J. Phys. Chem. C*, **119**, 4675 (2015).
37. K. Mahankali, N. K. Thangavel, and L. M. Reddy Arava, *Nano Lett.*, **19**, 5229 (2019).
38. T. Kai, C. G. Zoski, and A. J. Bard, *Chem. Commun.*, **54**, 1934 (2018).
39. F. Cao, J. Kim, and A. J. Bard, *J. Am. Chem. Soc.*, **136**, 18163 (2014).
40. B. R. Horrocks, D. Schmidtke, A. Heller, and A. J. Bard, *Anal. Chem.*, **65**, 3605 (1993).
41. M. V. Mirkin, H. Yang, and A. J. Bard, *J. Electrochem. Soc.*, **139**, 2212 (1992).
42. J. J. Chen, R. M. Yuan, J. M. Feng, Q. Zhang, J. X. Huang, G. Fu, M. S. Zheng, B. Ren, and Q. F. Dong, *Chem. Mater.*, **27**, 2048 (2015).
43. P. Bertoncello, *Energy Environ. Sci.*, **3**, 1620 (2010).

44. Z. Feng, C. Kim, A. Vijh, M. Armand, K. H. Bevan, and K. Zaghib, *J. Power Sources*, **272**, 518 (2014).
45. P. Partovi-Azar, T. D. Kühne, and P. Kaghazchi, *Phys. Chem. Chem. Phys.*, **17**, 22009 (2015).
46. G. Yang, S. Shi, J. Yang, and Y. Ma, *J. Mater. Chem. A*, **3**, 8865 (2015).
47. N. K. Thangavel, D. Gopalakrishnan, and L. M. R. Arava, *J. Phys. Chem. C*, **121**, 12718 (2017).
48. G. Babu, K. Ababtain, K. Y. Ng, and L. M. Arava, *Sci Rep.*, **5**, 8763 (2015).
49. M. Miroshnikov et al., *ACS Appl. Energy Mater.*, **2**, 8596 (2019).
50. K. Mahankali, N. K. Thangavel, Y. Ding, S. K. Putatunda, and L. M. R. Arava, *Electrochim. Acta*, **326**, 134989 (2019).
51. D. Moy, A. Manivannan, and S. Narayanan, *J. Electrochem. Soc.*, **162**, A1 (2015).
52. F. Y. Fan, W. C. Carter, and Y. M. Chiang, *Adv. Mater.*, **27**, 5203 (2015).
53. L. C. Gerber, P. D. Frischmann, F. Y. Fan, S. E. Doris, X. Qu, A. M. Scheuermann, K. Persson, Y. M. Chiang, and B. A. Helms, *Nano Lett.*, **16**, 549 (2016).
54. F. Y. Fan and Y. M. Chiang, *J. Electrochem. Soc.*, **164**, A917 (2017).
55. M. Cuisinier, P. E. Cabelguen, S. Evers, G. He, M. Kolbeck, A. Garsuch, T. Bolin, M. Balasubramanian, and L. F. Nazar, *J. Phys. Chem. Lett.*, **4**, 3227 (2013).
56. Y. Gorlin, M. U. Patel, A. Freiberg, Q. He, M. Piana, M. Tromp, and H. A. Gasteiger, *J. Electrochem. Soc.*, **163**, A930 (2016).
57. Z. Liu, D. Hubble, P. B. Balbuena, and P. P. Mukherjee, *Phys. Chem. Chem. Phys.*, **17**, 9032 (2015).
58. Z. Liu, P. B. Balbuena, and P. P. Mukherjee, *J. Phys. Chem. Lett.*, **8**, 1324 (2017).